COMPARISON OF ALSI10MG AND AL 6061 PROCESSED THROUGH DMLS

Benjamin A. Fulcher*, David K. Leigh*, Trevor J. Watt†

*Harvest Technologies, Belton, TX 76513
†Department of Mechanical Engineering, The University of Texas at Austin, Austin, TX 78712

Abstract

Direct Metal Laser Sintering (DMLS) processing of aluminum alloys has been primarily limited to a casting grade of aluminum, AlSi10Mg. The reasons for the choice of AlSi10Mg by machine manufacturers are presently unknown; however, it is suspected that the reduced coefficient of thermal expansion (CTE) due to the presence of Silicon may enhance DMLS processability. Aluminum 6061 (Al 6061) is a commonly used alloy across a wide range of industries and applications, and Harvest has observed a high interest in DMLS-manufactured Al 6061 products. However, the higher CTE value potentially presents greater challenges in controlling the shrinkage-induced warp common during DMLS. The work presented in this paper was performed in an effort to understand differences in manufacturability as well as mechanical properties of DMLS-processed AlSi10Mg and Al 6061.

1. Introduction

Casting, welding, and DMLS of aluminum alloys pose several challenges: First, aluminum rapidly forms an oxide layer when exposed to air which requires strong fluxes or an inert atmosphere. Second, water vapor or any adsorbed hydrogen-bearing species can result in hydrogen porosity during solidification, as molten aluminum has a high solubility limit for hydrogen which diminishes rapidly upon solidification. Third, aluminum has a high thermal diffusivity which requires a high energy input to overcome conductive cooling into the surrounding material. Some aluminum alloys (6xxx series in particular) are also susceptible to hot tearing and hot cracking in casting and welding processes. Fracture can occur in the solid-state due to thermal contraction (hot cracking), or above the solidus temperature due to solidification shrinkage (hot tearing).

AlSi10Mg is currently the most commonly used aluminum alloy in DMLS, presumably due to the ease of processing. Aluminum-silicon alloys are primarily used in castings due to their high melt fluidity and relatively low shrinkage [1, 2]. Adding more than a few percent of silicon to aluminum significantly improves these properties, reducing the likelihood of hot tearing during solidification. Lower shrinkage results in reduced strain levels and therefore less susceptibility to cracking during solidification. Furthermore, if the melt is fluid enough it is able to "heal", or back-fill, any cracks that form while the material is in its mushy state. Silicon, with a high heat of fusion, contributes to an alloy's fluid life by releasing heat into the melt during solidification, thereby slowing the solidification and reducing strain rate in the mushy zone.

Solidification range (ΔT, or $T_{liquidus}$ - $T_{solidus}$) is also relevant to hot tearing. A larger ΔT results in a greater chance for hot tearing because less liquid is available for interdentritic feeding when the material reaches the solidus or eutectic temperature. Near-eutectic alloys such as AlSi10Mg have a relatively low ΔT (40 K), whereas Al 6061 has a relatively large ΔT (70 K) which is further increased by non-equilibrium solidification and fast cooling rates and in DMLS. In casting processes, the hot tearing of aluminum alloys is reduced by increasing the mold temperature, and reducing the pour temperature [3]. The solidification range for an AlSi10 alloy is represented in the Al-Si binary phase in Figure 1, and the non-equilibrium solidification behavior of an Al-Mg alloy is displayed in Figure 2.
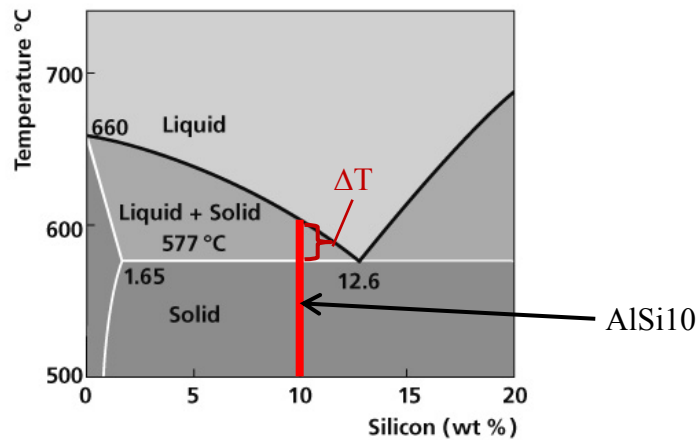

Figure 1. *Al-Si binary phase diagram illustrating thermal behavior of AlSi10 alloys [4]*
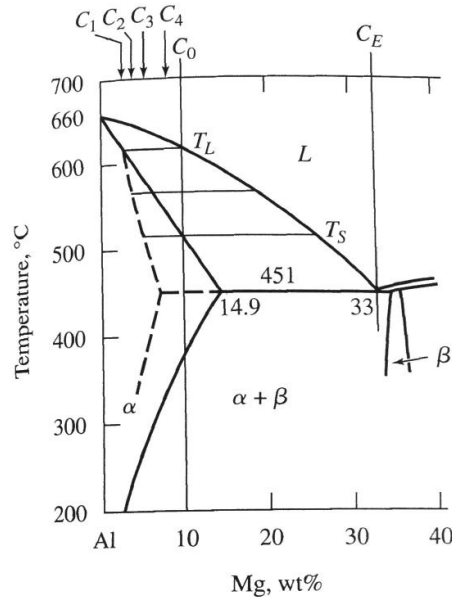

Figure 2. *Non-equilibrium solidification of an Al-Mg alloy with composition C_0. Solidification begins with the rejection of α solid-solution crystals. If time is insufficient for diffusion of Mg into the solidified core, microsegregation occurs and ΔT increases [5].*

Given the potential difficulties associated with processing Al 6061 in DMLS it is not surprising that it is not widely used in the additive manufacturing industry. However, Al 6061 is commonly used across multiple industries, is often used for CNC prototyping, and Harvest has observed a desire from aerospace customers for DMLS Al 6061 components.

2. Results and Discussion

Scan track testing was performed for Al 6061, AlSi10Mg microstructure and mechanical test samples were built according to the default EOS parameter set, and Al 6061 samples were built according to the parameters listed in Table 1. Note that two builds were performed in Al 6061, referred to as version 1 (v1) and version 2 (v2). The second build employed a preheat scan in an effort to alleviate cracking issues observed in the first build.

Table 1. *DMLS processing parameters used in this study*

	AlSi10Mg	Al 6061 (v1)	Al 6061 (v2)
Laser Power (W)	EOS_DirectPart	370	70 / 370
Scan Speed (mm/s)	EOS_DirectPart	940	3,000 / 940
Scan Spacing (mm)	EOS_DirectPart	0.19	.19
Layer Thickness (µm)	30	30	40
Platform Temperature (ºC)	30	30	80

2.1. Al 6061 Scan Track Testing

Prior to building test samples in Al 6061, a scan track design of experiments was performed to provide a general idea of appropriate scan speed and laser power. In the first scan track test, laser power (P) was varied from 70 to 370 W and scan speed (S) was varied from 1000 to 3000 mm/s. In the second scan track test, the laser power was varied from 270 to 370 W and the scan speed was varied from 500 to 1500 mm/s. Scan spacing was left at the default EOS value for AlSi10Mg of 0.19 mm. The tracks were examined under microscope and characterized by appearance. The following descriptions explain the characters used in Table 2 and Table 3.

- U – Un-melted
- X – Balling, broken tracks, unconnected tracks
- Y – Balling, unconnected tracks
- Z – Balling with connected tracks
- R – Rough with connected tracks
- A – Smooth with connected tracks

In Table 2 and Table 3, the lower-left corner corresponds with the highest laser energy input and the upper-right corner corresponds with the lowest energy input. The best results in the two studies tend toward higher laser energy.

Table 2. *First Al 6061 scan track test*

Test #1		Power (W)				
		370	295	220	145	70
Speed (mm/s)	3000	X	X	X	X	U
	2500	Y	Y	X	X	U
	2000	Z	Y	X	X	U
	1500	Z	Z	Y	X	U
	1000	A	R	Y	Y	X

Table 3. *Second Al 6061 scan track test*

Test #2		Power (W)				
		370	345	320	295	270
Speed (mm/s)	1500	Z	Z	Y	Y	Y
	1250	Z	Z	R	R	Y
	1000	A	R	R	R	R
	750	A	A	A	A	R
	500	A	A	A	A	A

After performing the scan track testing, laser power of 370 W and scan speed of 940 mm/s were chosen for the first Al 6061 build. This combination ensures good melt characteristics while the relatively high scan speed facilitates a fast build rate. As previously mentioned, a second build was run after the first in order to alleviate cracking issues observed in the first build (see section 2.2). The second build employed a preheat scan of 70 W at 3,000 mm/s which corresponds with an un-melted track in the scan track testing. Figure 3 displays three representative scan tracks from the first test.
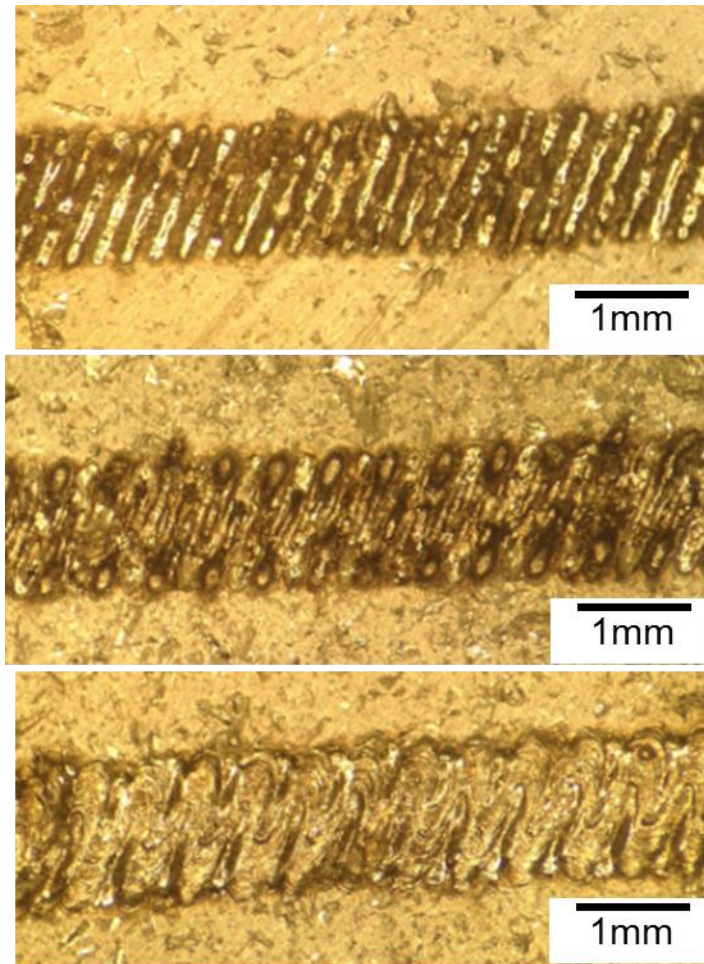
Figure 3. *(upper) Al 6061 scan track testing at P=220 W, S=1000 mm/s (type Y); **(middle)** P=370 W, S=2000 mm/s (type Z); **(lower)** P=370 W, S=1000 mm/s (type A)*

2.2. Microstructural Comparison

Specimens were sectioned with a low-speed diamond saw and encapsulated in epoxy. Each epoxy-mounted specimen was sequentially ground using a rotary polisher with 400, 600, 1200 and 4000 grit SiC papers immersed in water, then sequentially polished with 9-μm, 3-μm, and 1-μm diamond suspensions. Final polishing used a 0.04-μm colloidal silica suspension. The specimens were rinsed with water and ethanol and air-dried between each grinding/polishing step.

Specimens were etched using one of two techniques: The first technique used 2% aqueous fluoroboric acid (HBF_4, "Barker's reagent") for approximately 60 seconds, which resulted in tint etching of the AlSi10Mg and precipitate etching of the Al 6061. The second technique used the same reagent with an electrical current applied at 25 VDC with the specimen as the anode. This electrochemical etching results in grain orientation coloring when viewed with an optical microscope equipped with cross-polarized filters and a λ tint plate. After etching, specimens

were analyzed using a Zeiss Axiovert 405M optical polarizing microscope, and a JEOL JSM-5610 scanning electron microscope equipped with energy dispersive spectroscopy (EDS).

2.2.1. As-built Cross-Section Images

The following images were taken of material in the as-built (melted, stress relieved) condition.

AlSi10Mg as-built micrographs

Optical microscope images of electrolytic etched AlSi10Mg in the as-built condition are shown in Figure 4. In general there is little difference between the different melt pools. Melt pool edges are tinted yellow or blue, with the central region colored magenta. The melt pool boundaries are extremely well defined and there is sporadic evidence of epitaxial solidification. In Figure 5 epitaxial solidification is evident in the middle of the melt pools as propagation of the same color, though the melt pool edges tend to show greater orientation contrast.

Figure 4. *Optical micrographs of as-built AlSi10Mg,electrolytic etch; XY plane (left), and XZ plane (right)*
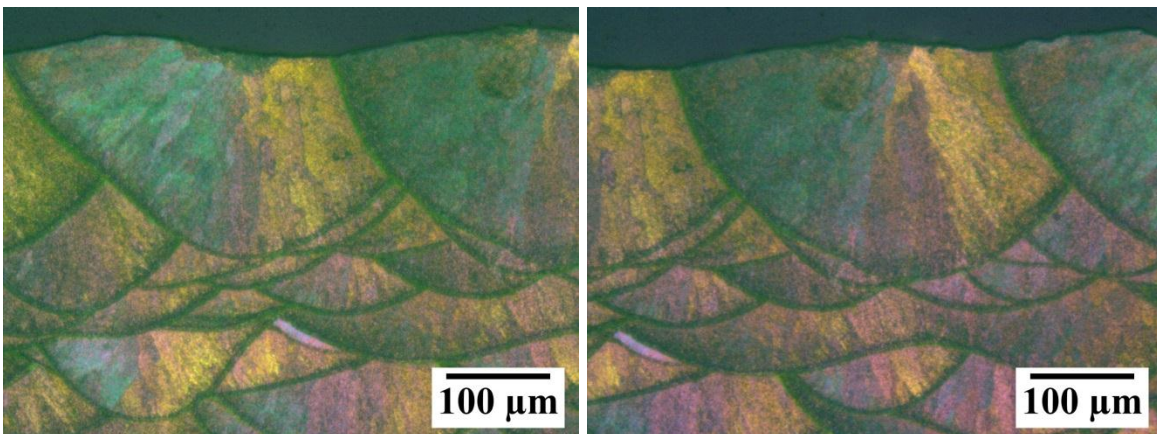

Figure 5. *Optical micrographs of as-built AlSi10Mg, electrolytic etch; XZ plane*

SEM images of the XY plane for AlSi10Mg in Figure 6 show a cellular solidification structure with cells approximately 0.4-0.5 μm in size. The cells increase in size up to about 1 μm at the melt pool boundaries. These larger cells are likely HAZ material that has been heated up to just below the melting temperature, resulting in coarsening of the microstructure. This region is surrounded on one side by a 2-3 μm band of detached dendrites/cells. Beyond this band the melt pools develop a "honeycomb" style inter-connected microstructure.

Figure 6. *SEM images of AlSi10Mg as-built, chemical etch; XY plane*

In Figure 7, the cells in the XZ plane show some evidence of epitaxial solidification near the melt pool bottoms, though the sides of the melt pools tend to have non-epitaxial cells aligned in the direction of greatest heat transfer. The detached cells seen in the XY plane are observed on the underside of the coarsened cells. Since these are evident as spots in both the XY and XZ plane, it is apparent that they are actually nodular in shape. Additional analysis is needed to determine if this is due to solidification of the original melt pool or heating from the overlapping melt pool, though it is likely the latter.
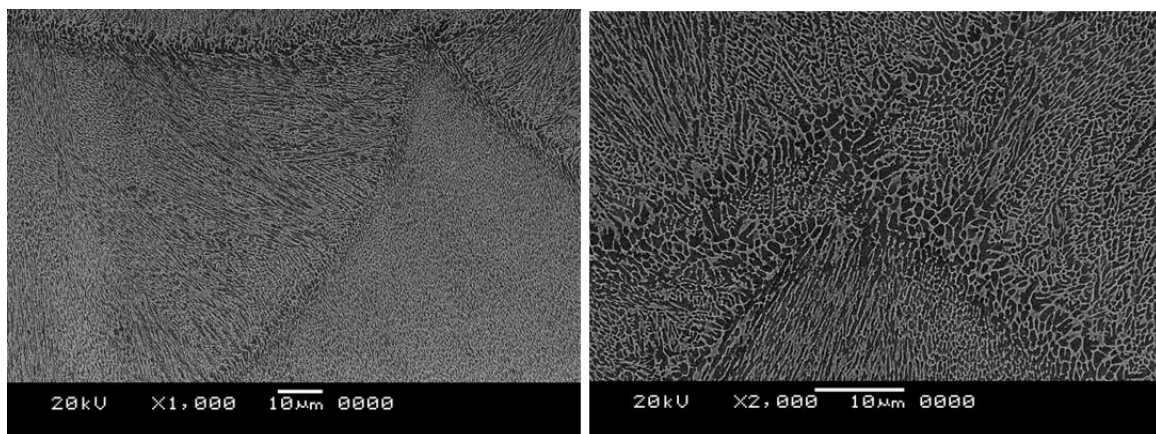

Figure 7. *SEM images of AlSi10Mg as-built, chemical etch; XZ plane*

Al 6061 (v1) as-built micrographs

Images of as-built, polished Al 6061 (v1) samples are shown in Figure 8. Significant cracking and porosity is observed throughout the material. The cracks in the XY plane are arranged in a "mud crack" fashion suggesting biaxial tensile stresses, and are often coincident with pores.
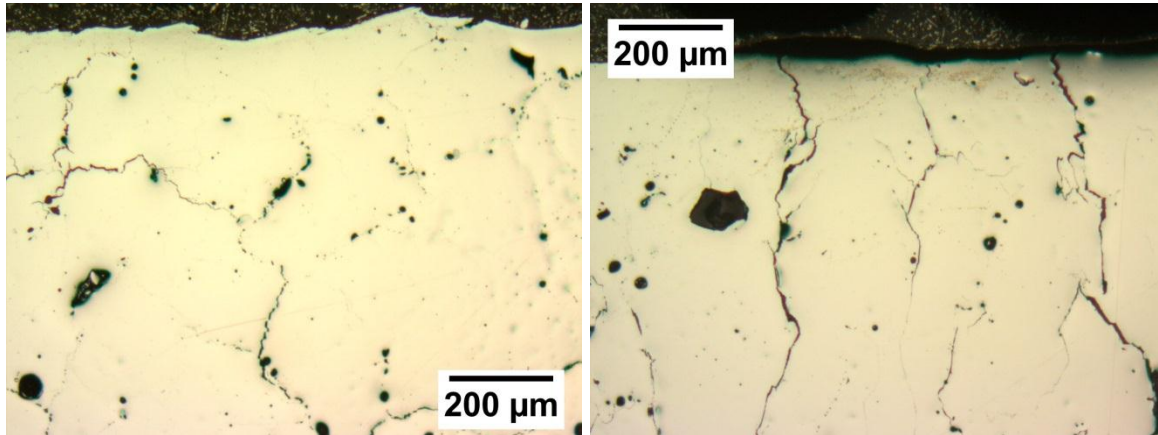

Figure 8. *As-built, polished Al 6061 (v1) XY plane (left) and XZ plane (right)*

Figure 9 is an SEM image of a crack in the as-built Al 6061 in the XY plane. Tendrils that connect opposing crack faces suggest that fracture occurred when this material was still in the "mushy" state, or between the solidus and liquidus temperatures.
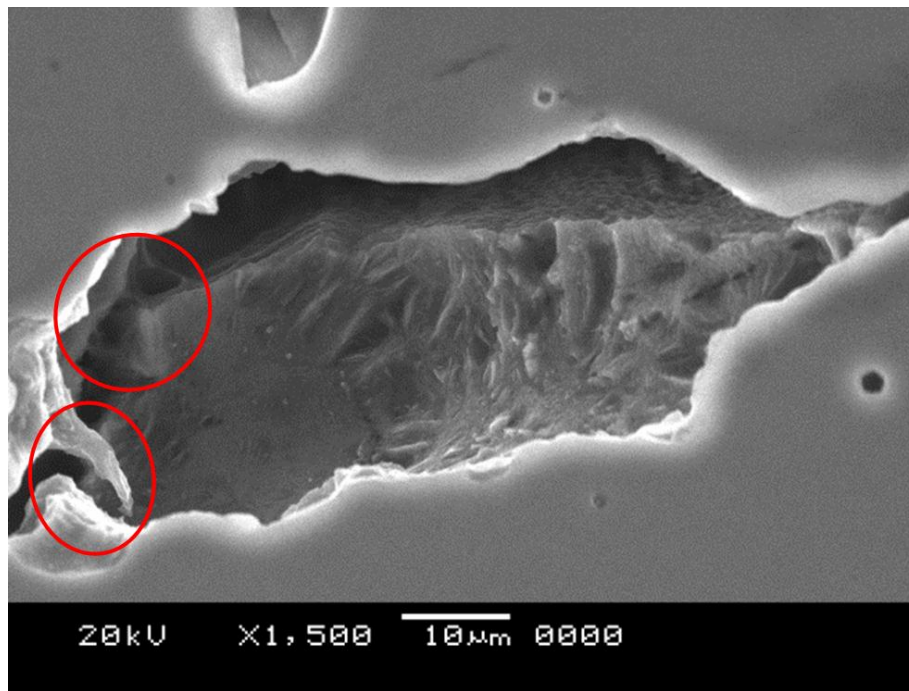

Figure 9. *SEM image of Al 6061(v1) crack in the XY plane*

411

In Figure 10, melt pool boundaries are revealed as well as grain orientation contrast for the as-built Al 6061. Epitaxial solidification is clearly evident for the Al 6061, unlike the AlSi10Mg. Grain orientations span many build layers and can consume large portions of a particular melt pool's width. Cracks are predominately intergranular in nature – this behavior is expected from the previous figure which showed evidence of hot tearing in the fracture surfaces. However, unlike traditional hot tearing which is due to macroscopic geometric constraints, the cracks observed here occur on a much smaller length-scale and occur throughout the melt pool. Cracks also tend to correspond with greater changes in grain color (grain orientation), which suggests that fracture is due to anisotropic contraction during solidification and cooling. The cracking is remarkably consistent along the Z axis and spans across multiple powder layers.
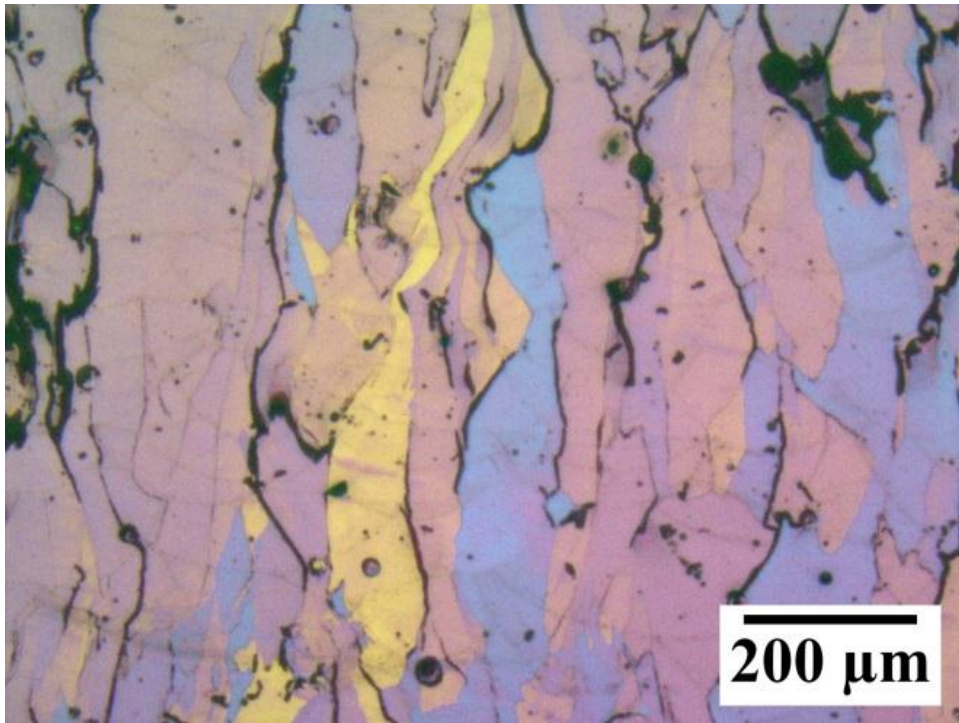

Figure 10. *Optical micrograph of Al 6061 (v1) as built, electrolytic etch; XZ plane*

Al 6061 (v2) as-built micrographs

The second build of Al 6061 (with preheat scanning) shows marked improvement over the first build, although there is still work to be done to completely eliminate cracking and porosity. The preheat scan effectively reduces thermal gradients during cooling and thereby reduces thermal cracking. While there are some regions of significant cracking in the second build of Al 6061, most of the material exhibits only fine-scale cracks that are difficult to see without using dark-field imaging.
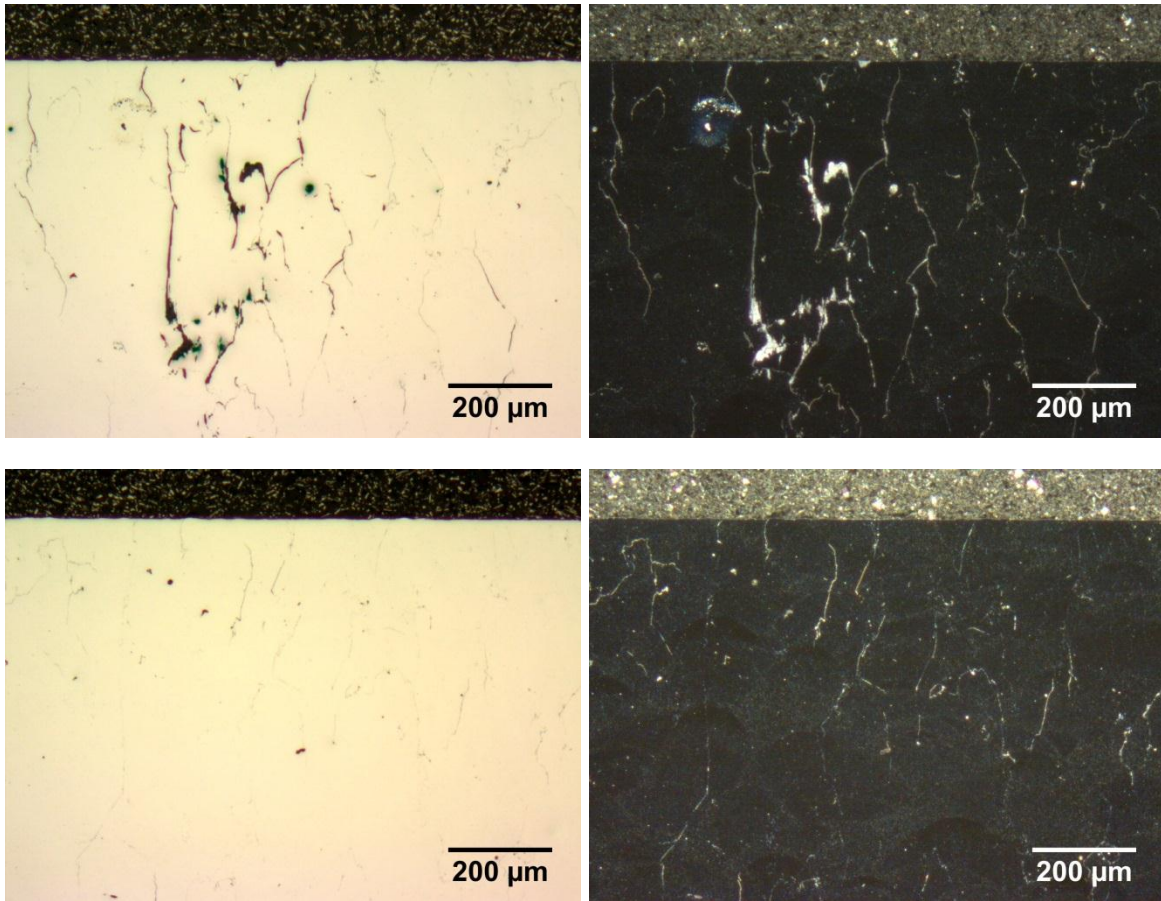
Figure 11. *Optical micrographs of Al 6061 (v2) as-built, polished; XZ plane. Bright-field images are shown on the left with corresponding dark-field images on the right.*

2.2.2. Heat-Treated Cross-Section Images

The following images were taken of material in the as-built (melted, stress relieved), and heat treated (HIP, solutionized, aged) condition.

<u>AlSi10Mg heat-treated micrographs</u>

The XY plane micrographs of the heat-treated AlSi10Mg in Figure 12 show that the original cellular microstructure has been converted into coarsened nodular particles. Furthermore, the grain orientation no longer follows the melt pools as in the as-built condition. The XZ plane micrographs in Figure 13 show some particles aligned along previous cellular growth directions. The grain orientation is irregular, and does not consistently span multiple powder layers as in the Al 6061.
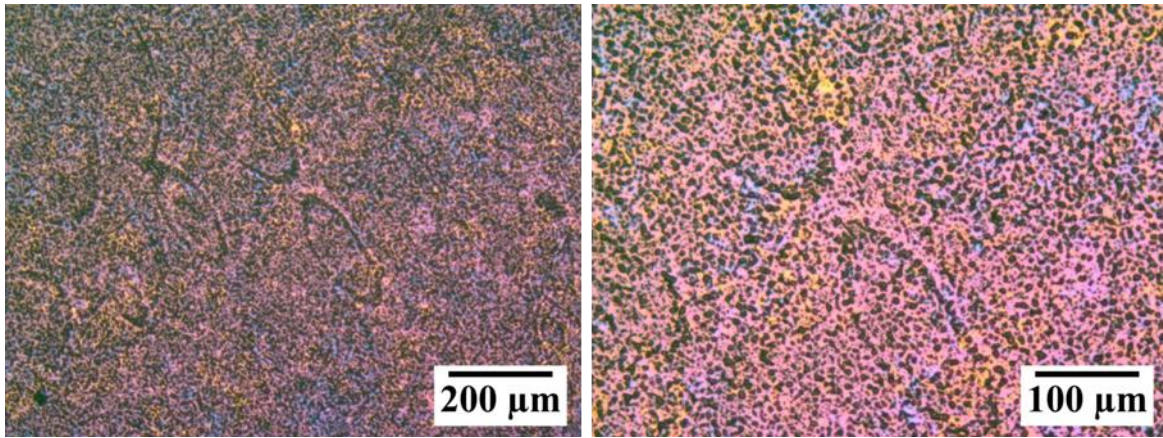
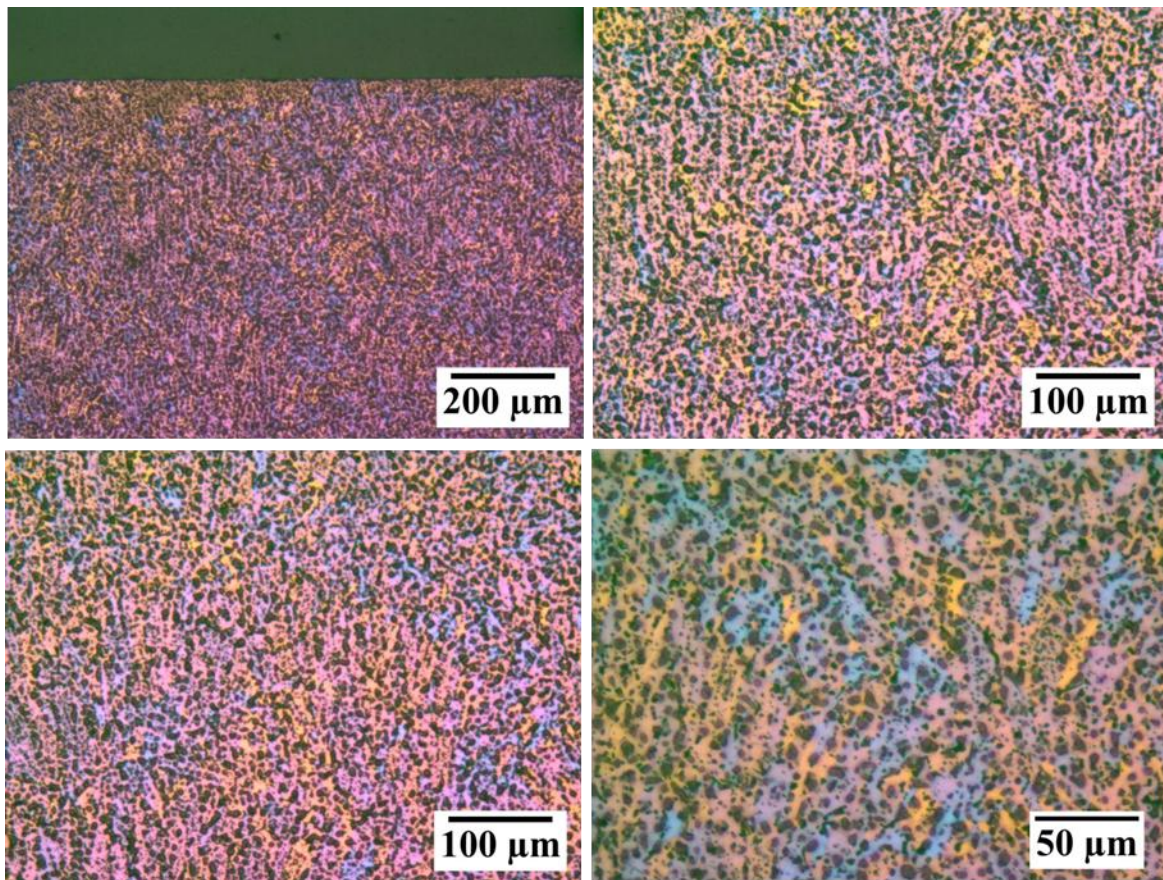**Figure 12.** *Optical micrograph of AlSi10Mg-T6, electrolytic etch; XY plane*

Figure 13. *Optical micrograph of AlSi10Mg-T6, electrolytic etch; XZ plane*

Al 6061 (v1) heat-treated micrographs

Figure 14 shows that grain orientation is largely consistent across the XY plane, and the cracks no longer correspond with significant changes in grain orientation. The micrograph in Figure 15 is similar to the as-built Al 6061 (see Figure 10), though the pool boundaries are

414

largely absent. This confirms that pool boundaries were originally marked by coarsened precipitates (presumably Mg2Si) that have been dissolved and redistributed as smaller dispersed precipitates due to the T6 heat treatment.
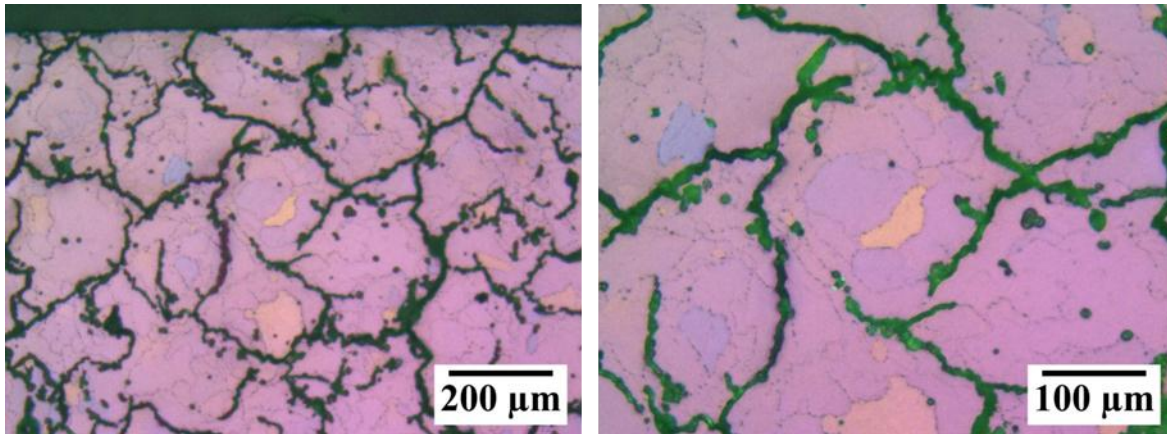

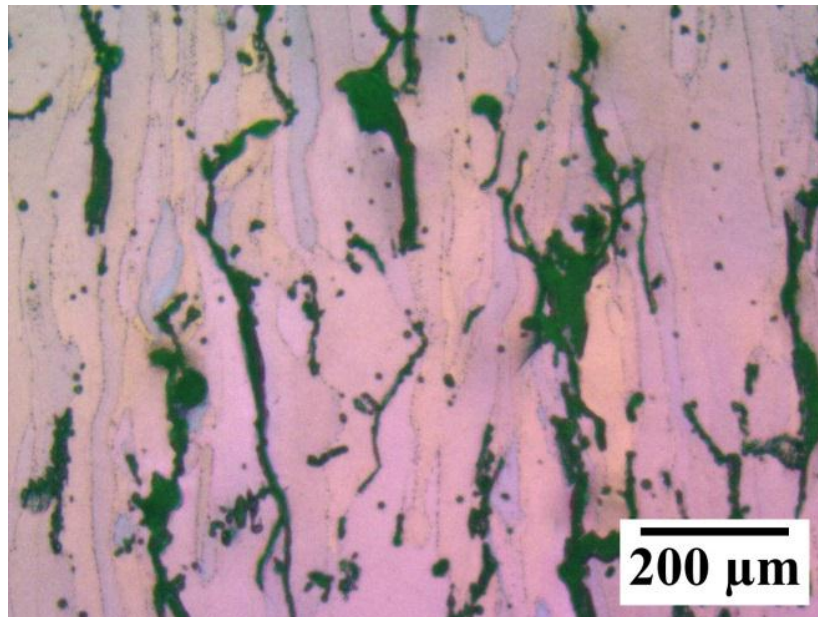**Figure 14.** *Optical micrographs of Al 6061-T6, electrolytic etch; XY plane*

Figure 15. *Optical micrograph of Al 6061-T6, electrolytic etch; XZ plane*

2.3. Mechanical Properties Comparison

Tensile bars and Charpy impact samples were built in AlSi10Mg and Al 6061. Tensile bars were built according to ASTM E8 (half size) along the X axis and the Z axis. Hand finishing was performed on the X tensile bars in order to remove support structure residue, and no finishing was performed on the Z tensile bars. Charpy specimens were built and the notch was subsequently machined. As seen in Table 4, mechanical properties for the Al 6061 specimens are

highly anisotropic. The Z specimens exhibit much higher UTS and impact energies than the X specimens, however even the Z properties are much lower than expected. These results are preliminary and should improve with future parameter optimization efforts. Fracture surfaces of the Charpy samples can be seen in Figure 16. The anisotropy in the Al 6061 is evident in these images as well, and there is little observable difference between the X and Z fracture surfaces for the AlSi10Mg. At the time this report was written, mechanical testing of Al 6061 (v2) had not yet been performed.

Table 4. *UTS and impact energy for AlSi10Mg and Al 6061 specimens*

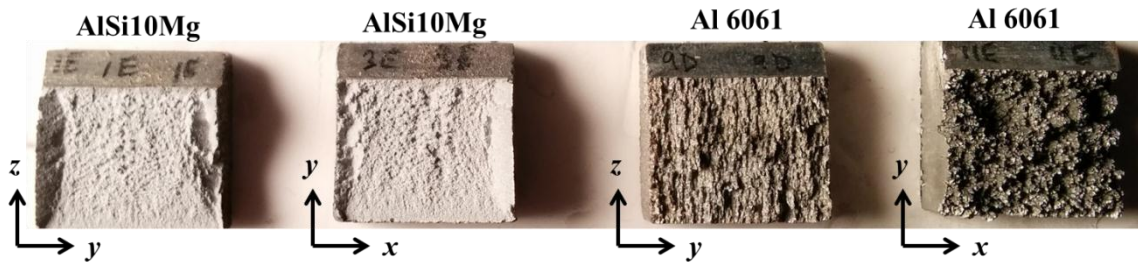|	AlSi10Mg, X-Up	AlSi10Mg, Z-Up	Al 6061, X-Up (v1)	Al 6061, Z-Up (v1)	Al 6061 (v2)
UTS (ksi)	48.7	43.9	6.1	33.4	*In process*
Impact Energy (J)	4	4	1.5	7	*In process*
Condition	HIP, T6	HIP, T6	HIP, T6	HIP, T6	-

Figure 16. *Fracture surfaces of AlSi10Mg Charpy Specimens*

SEM images of the fracture surfaces of AlSi10Mg-T6 Charpy bars built along the X and Z axes are shown in Figure 17. These surfaces reveal traditional ductile fracture through micro-void coalescence. Once again, there is little observable difference between the X and Z fracture surfaces.
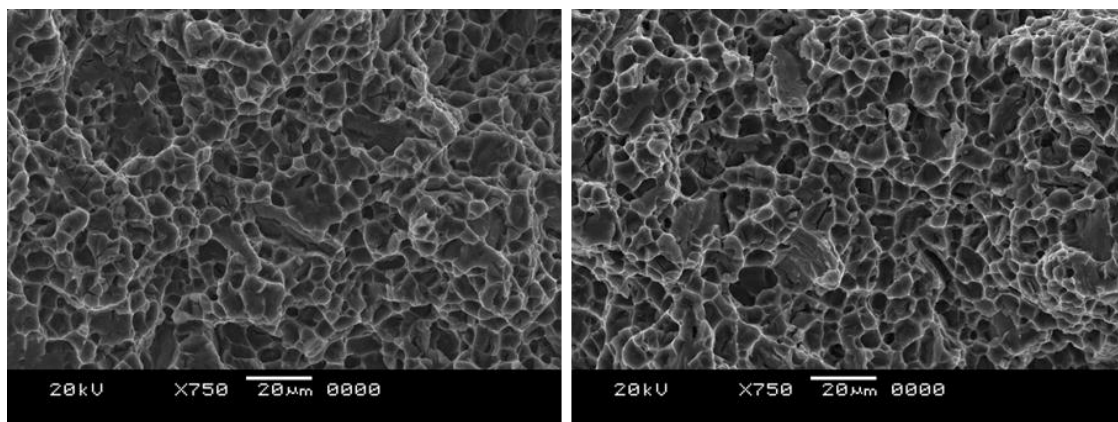

Figure 17. *SEM images of AlSi10Mg-T6 Charpy fracture surfaces; (left) X-Up and (right) Z-Up*

The fracture behavior for the Al 6061 (v1) material is markedly different than that of the AlSi10Mg. This material fails in a manner similar to directional fibrous composites. Sudden changes in the fracture surface orientation and texture seen in Figure 18 are likely due to residual melt pool boundaries, where certain grain orientations change the direction of growth as shown in the previous color metallography images. The columnar fracture surfaces indicate that the original microstructure underwent cellular solidification similar to the AlSi10Mg. Delamination appears to be the dominant failure mechanism for both the X-up and Z-up Charpy specimens. SEM images of the Z-up fracture surface can be seen in Figure 19.
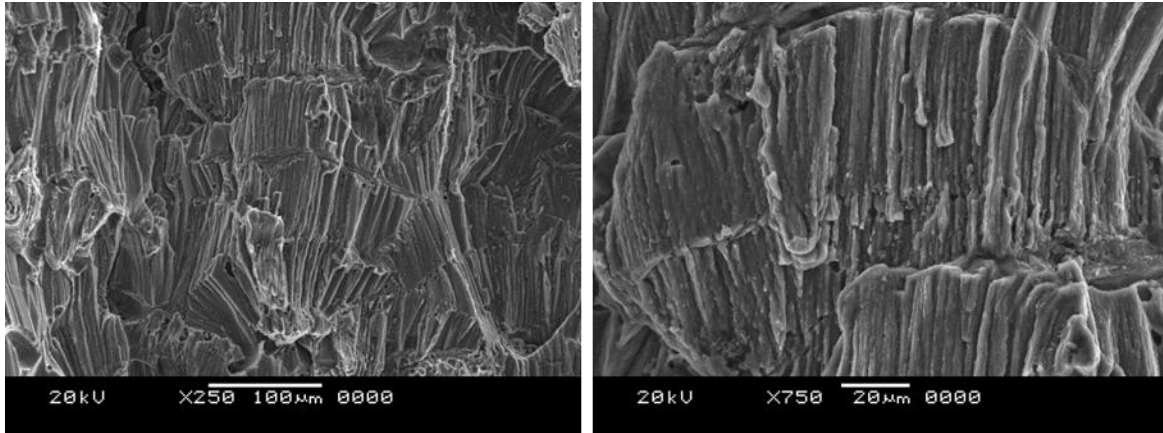

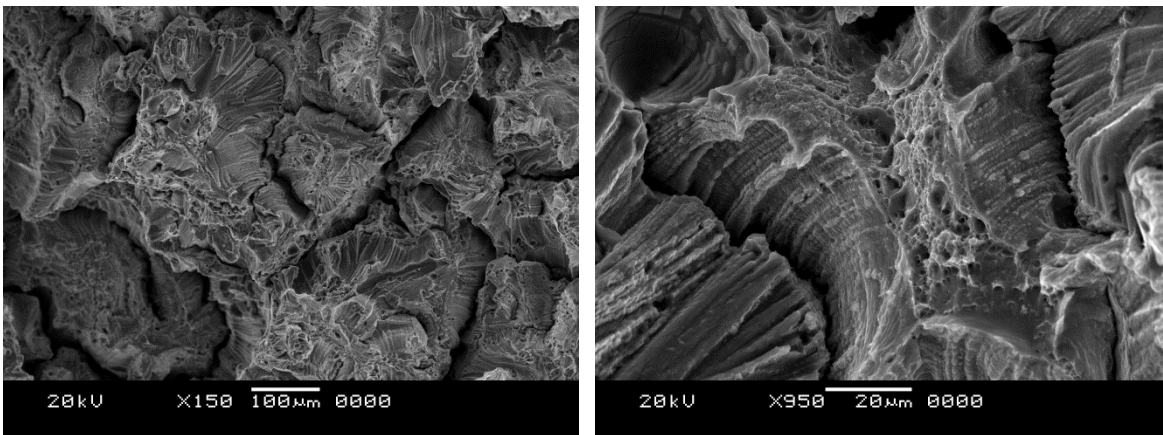**Figure 18.** *SEM images of Al 6061-T6 X-Up Charpy fracture surface*

Figure 19. *SEM images of Al 6061-T6 Z-Up Charpy fracture surface*

3. Conclusions and Recommendations

The AlSi10Mg samples manufactured, heat-treated and tested in this work displayed relatively isotropic properties. The Al 6061 samples, however, were highly anisotropic and behaved similarly to fibrous composites. This behavior is not surprising considered the tendency of Al 6061 to hot tear during traditional casting and welding processes. A second build of

417

Al 6061 with pre-heat laser scanning produced parts with significantly alleviated cracking, however more work needs to be performed to completely eliminate cracking concerns.

As a first effort to eliminate the cracking issues seen in Al 6061, a microstructure sample design of experiments should be performed with varying laser power and speed to determine whether an optimal range of scanning parameters exists. If optimizing a single pass is insufficient to alleviate cracking concerns, subsequent optimization of a pre-heat scan could be performed as well.

Another potential method to alleviate cracking is raising the platform temperature analogous to increasing the mold temperature in castings. Raising the platform temperature reduces thermal gradients during solidification, reducing thermally-induced stresses. Furthermore, increasing the platform temperature slows the rate of cooling, thereby reducing the microsegregation associated with non-equilibrium solidification. This could be a benefit if liquation cracking was an issue for the Al 6061 samples discussed in this report. The following graph presents the benefit of increasing mold temperature for an aluminum alloy.
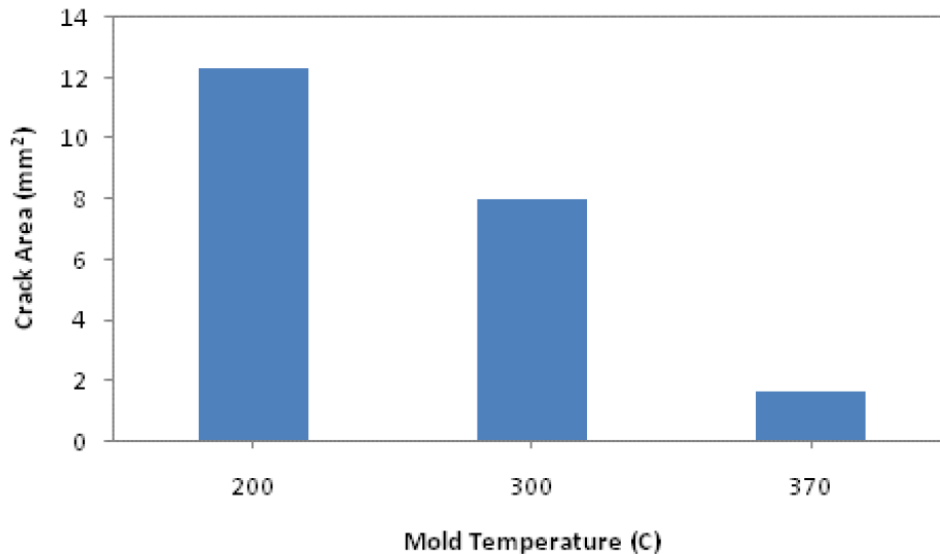

Figure 20. *Benefit of raising mold temperature in casting of Al alloys [3]*

References

[1] J. Davis, Metals Handbook Desk Edition, ASM International, 1998.

[2] D. Apelian, Aluminum Cast Alloys: Enabling Tools for Improved Performance, Wheeling, IL: North American Die Casting Association, 2009.

[3] S. Li, "Hot Tearing in Cast Aluminum Alloys: Measures and Effects on Process Variables," 2010.

[4] "Aluminium Brazing News, Knowledge & Technology," 29 September 2010. [Online]. Available: http://www.aluminium-brazing.com/2010/09/. [Accessed 2 August 2014].

[5] J. A. Schey, Introduction to Manufacturing Processes, Third ed., McGraw-Hill Higher Education, 2000, p. 155.